Thermal considerations in electrically-pumped metallo-dielectric nanolasers

Janelle Shane[1], Qing Gu[1], Felipe Vallini[2], Brett Wingad[1], Joseph S. T. Smalley[1], Newton C. Frateschi[2], and Yeshaiahu Fainman[1]

[1]University of California San Diego, 9500 Gilman Drive, La Jolla, USA;[2]University of Campinas, UNICAMP, Campinas, Brazil

ABSTRACT

Metal nanocavity-based lasers show promise for dense integration in nanophotonic devices, thanks to their compact size and lack of crosstalk. Thermal considerations in these devices have been largely overlooked in design, despite the importance of self-heating and heat dissipation to device performance. We discuss the sources of self-heating in electrically-pumped wavelength-scale nanolasers, and the incorporation of these heat sources into a heat dissipation model to calculate laser operating temperature. We apply this thermal model to an example electrically-pumped nanolaser operating at room temperature.

1. INTRODUCTION

Metal-clad subwavelength semiconductor lasers (here, referred to as MCSELs) have shown promise for chip-scale integration of compact, densely spaced laser sources, thanks to the high mode confinement provided by their metal cladding.[1,2] Lasing has been demonstrated in devices that are smaller than their free-space emission wavelengths in all three dimensions,[3,4] opening new avenues of research on the physics particular to small laser cavities.[5–8] Recently, room-temperature electrically-pumped lasing has been demonstrated in these devices,[9] beginning the transition of MCSELs from the first proof-of-concept devices to optical sources suitable for large-scale integration.

As MCSEL performance and reliability continue to improve, and as novel geometries continue to be explored, it becomes increasingly important to consider multiple aspects of nanolaser design, rather than focusing on cavity electromagnetic properties. Other important aspects of nanolaser design include surface passivation to reduce non-radiative surface recombination,[10,11] reducing material damage during fabrication,[12] and efficient use of available material gain.[13]

In this manuscript, we focus on thermal considerations, including self-heating and heat dissipation. Despite their importance in limiting device performance, the thermal properties of MCSELs have received little attention to date. The ability to model the laser's operating temperature allows the evaluation of the impact of self-heating on laser performance, as well as the design of new lasers with improved thermal properties. We present here a simple thermal modelling analysis that takes into account multiple sources of self-heating, and apply this model to an example MCSEL. In Section 2, we give an overview of the thermal modelling strategy that will be discussed in this paper, and present the example MCSEL design to which we will be applying this model. In Section 3, we adapt thermal models from vertical cavity surface emitting lasers (VCSELs) to include additional self-heating sources resulting from non-radiative carrier recombination: surface recombination and Auger recombination. We apply this model to calculate the total self-heating in an example MCSEL. In Section 4, we discuss the modeling of heat transport and dissipation in a nanolaser cavity, and apply this model to calculate the operating temperature of the example MCSEL analyzed in the previous section. In Section 5, we discuss the limitations of this thermal analysis and future improvements that might be made to increase accuracy.

Physics and Simulation of Optoelectronic Devices XXII, edited by Bernd Witzigmann, Marek Osinski, Fritz Henneberger, Yasuhiko Arakawa, Proc. of SPIE Vol. 8980, 898027 · © 2014 SPIE
CCC code: 0277-786X/14/$18 · doi: 10.1117/12.2057412

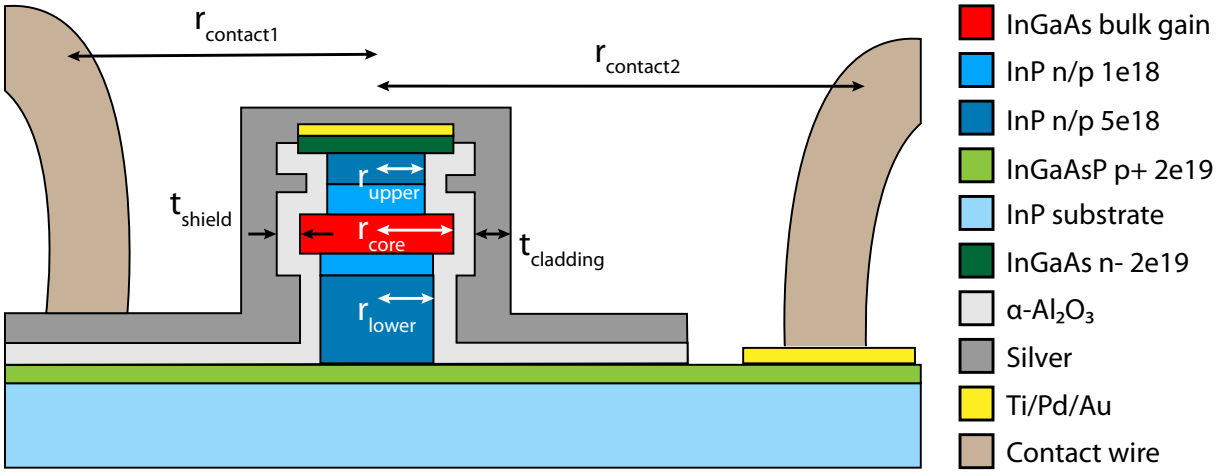

Figure 1.

Diagram of electrically-pumped nanolaser to be analyzed. The laser has an InGaAs gain region of radius r_{core} surrounded by a lower InP plug of radius r_{lower} and upper InP plug of radius r_{upper}. The laser is surrounded by a dielectric shield of amorphous Al_2O_3 (α-Al_2O_3), of thickness t_{shield}, which is in turn surrounded by a metal cladding layer (silver) of thickness $t_{cladding}$. The metal cladding layer connects the laser's InGaAsP top contact layer to the top electrical contact wire, at a distance $r_{contact1}$ from the laser's center. The bottom contact InGaAsP layer is connected to the bottom electrical contact wire at a distance $r_{contact2} \gg r_{contact1}$.

2. THERMAL MODEL OVERVIEW

The thermal modelling strategy described in this paper is based on models used in VCSELs,[14] with modification to include features specific to nanoscale lasers. In the first step, detailed in Section 3, we calculate the total self-heating power generated by the laser at a given operating current and operating temperature. These self-heating sources are located within the laser's semiconductor layers, as well as at the semiconductor junctions. In the second step, described in Section 4, we use finite element simulation to model the temperature distribution throughout the laser and surrounding substrate/cladding, for the self-heating sources calculated above. In our example, the temperature increases are moderate, so we calculate steady-state operating temperature given the self-heating sources and material thermal parameters at the laser's initial temperature. For a more complete analysis, necessary for a device where the temperature changes are very significant, this process should be performed iteratively, with the self-heating sources and operating temperature recalculated at each time step.

We apply this thermal analysis to the example MCSEL shown in Figure 1. The laser is based on the same epitaxially-grown wafer stack as used in previous work.[1,3] The gain layer is InGaAs lattice-matched to InP, with radius r_{core}. The radii and thicknesses of the other layers comprising the InP pedestals and InGaAsP top and bottom contact layers are given in Table 1. This laser's upper and lower InP pedestals both have radii less than r_{core}, due to a two-step etching process that increases modal confinement to the gain layer by undercutting the pedestals.[1] The etching rate is different depending on layer composition and doping, so the upper plug radius r_{upper} is smaller than the lower plug radius r_{lower}. The layer radii are measured from SEM images of a fabricated structure, although the sidewalls have an idealized vertical shape.

The laser is surrounded by a dielectric shield of amorphous Al_2O_3 (α-Al_2O_3) of thickness $t_{shield} = 168$ nm, which is in turn surrounded by a metal cladding layer (silver) of thickness $t_{cladding} = 258$ nm around the gain region. In this laser design, the distance $r_{contact1}$ of the top contact wire from the center of the laser is 20 μm, while the bottom contact wire is a far enough distance $r_{contact2} \gg r_{contact1}$ from the laser's center that it does not play a role in heat dissipation.

3. SELF-HEATING SOURCES

Our first step in determining the nanolaser's operating temperature is to determine the amount and location of the nanolaser's self-heating sources. Following the effective heat source model used for VCSELs,[14] the major

Table 1.
Dimensions of MCSEL laser simulated in this paper. The layer compositions, doping, and thicknesses are those of the InP/InGaAs/InP double heterostructure grown on InP, used in previous work.[1,3] The layer radii are for an example nanolaser geometry, based on the SEM-measured dimensions of an experimentally-fabricated nanolaser. Conductivities are calculated from the doping level and carrier mobility using Equation 3.

Layer	Material	doping	Thickness	Radius	Carrier mobility	Conductivity
Top contact	InGaAs, n-	2e19 cm^{-3}	125 nm	574 nm	2.5e3$\left(\frac{cm^2}{V*s}\right)^{15}$	8.011e5 S/m
Upper pedestal top	InP, n	5e18 cm^{-3}	235 nm	358 nm	1.25e3 $\left(\frac{cm^2}{V*s}\right)^{16}$	1.001e5 S/m
Upper pedestal bottom	InP, n	1e18 cm^{-3}	235 nm	358 nm	2e3 $\left(\frac{cm^2}{V*s}\right)^{16}$	3.204e4 S/m
Gain	InGaAs bulk	-	300 nm	574 nm	-	-
Lower pedestal top	InP, p	1e18 cm^{-3}	125 nm	431 nm	80 $\left(\frac{cm^2}{V*s}\right)^{16}$	1.282e3 S/m
Lower pedestal bottom	InP, p	5e18 cm^{-3}	725 nm	431 nm	35 $\left(\frac{cm^2}{V*s}\right)^{16}$	2.803e3 S/m
Bottom contact	InGaAsP, p+	2e19 cm^{-3}	135 nm	N/A	50 $\left(\frac{cm^2}{V*s}\right)^{15}$	1.602e4 S/m

sources of self-heating are Joule heating, junction heating, and heterojunction heating, which are calculated as described below. To these self-heating sources we add heat generated by non-radiative recombination; namely, surface and Auger recombination heating. Surface recombination heating is important in lasers with nanoscale gain regions, and Auger recombination heating is important at high carrier concentrations. These self-heating terms are dependent on operating current as well as on ambient temperature.

Most of the heat source calculations described below depend on the nanolaser's electronic behavior. To perform these electronic simulations, we use SILVACO's ATLAS, a 2D electronic device simulator that self-consistently solves the Poisson equation, the Schrödinger equation, and the carrier transport equation to calculate voltage, carrier density, and quasi-Fermi level separation. The results from these electronic simulations, for the nanolaser described in Figure 1 and Table 1, are shown in Figure 2.

3.1 Joule heating

Joule heating is self-heating due to the resistance of each of the semiconductor layers, and is given by

$$Q_J = I^2 R_s \tag{1}$$

where I is the operating current and R_s is the stack resistance of the semiconductor layer. The stack resistance of the ith layer may be calculated from the layer's radius r_i, thickness t_i, and conductivity σ_i using the standard formula for stack resistance,[14]

$$R_i = \frac{t_i}{\sigma_i \pi (r_i)^2} \tag{2}$$

The material conductivity of the ith layer may be calculated using

$$\sigma_i = n_i \mu_i q_e \tag{3}$$

where n_i is the doping level, μ_i is the carrier mobility, and q_e is the electron charge.

The bottom contact layer behaves like a cylindrical thin film contact geometry. The resistance in this layer is given by[17]

$$R_{bc} = \frac{1}{2\pi\sigma_{bc}t_{bc}} \ln\left(\frac{r_{bc}}{r_{lp}}\right) + \frac{1}{4\sigma_{bc}r_{lp}} \bar{R}_c\left(\frac{r_{lp}}{t_{bc}}, \frac{\sigma_{bc}}{\sigma_{lp}}\right) \tag{4}$$

where the first term is the resistance of the bottom contact layer region between the nearest contact wire and the laser's lower pedestal, and the second term is the resistance of the bottom contact layer directly underneath the laser's lower pedestal. r_{lp} is the radius of the lower pedestal and r_{bc} is the distance between the laser's center

and the nearest contact wire. For our laser, $r_{lp} = r_{lower}$ and $r_{bc} = r_{contact1}$ as drawn in Figure 1. σ_{bc} is the conductivity of the bottom contact layer, while σ_{lp} is the conductivity of the laser's lower pedestal. An empirical expression for $\bar{R}_c$ is numerically found to be[17]

$$\bar{R}_c\left(\frac{r_{lp}}{t_{bc}}, \frac{\sigma_{bc}}{\sigma_{lp}}\right) \cong \bar{R}_{c0}\left(\frac{r_{lp}}{t_{bc}}\right) + \frac{\Delta\left(\frac{r_{lp}}{t_{bc}}\right)}{2} \cdot \frac{2\sigma_{bc}}{\sigma_{bc} + \beta\left(\frac{r_{lp}}{t_{bc}}\right)\sigma_{lp}} \tag{5}$$

where $\bar{R}_{c0}\left(\frac{r_{lp}}{t_{bc}}\right)$ and $\Delta\left(\frac{r_{lp}}{t_{bc}}\right)$ are defined differently depending on the ratio $\frac{r_{lp}}{t_{bc}}$.

For $0.0011 \leq \frac{r_{lp}}{t_{bc}} \leq 1$ (lower pedestal radius is less than bottom contact thickness),

$$\bar{R}_{c0}\left(\frac{r_{lp}}{t_{bc}}\right) = 1 - 2.2968\left(\frac{r_{lp}}{t_{bc}}\right) + 4.9412\left(\frac{r_{lp}}{t_{bc}}\right)^2 - 6.1773\left(\frac{r_{lp}}{t_{bc}}\right)^3 + 3.811\left(\frac{r_{lp}}{t_{bc}}\right)^4 - 0.8836\left(\frac{r_{lp}}{t_{bc}}\right)^5$$

$$\Delta\left(\frac{r_{lp}}{t_{bc}}\right) = 0.0184\left(\frac{r_{lp}}{t_{bc}}\right)^2 + 0.0073\left(\frac{r_{lp}}{t_{bc}}\right) + 0.0808$$

while for $1 < \left(\frac{r_{lp}}{t_{bc}}\right) < 10$ (lower pedestal radius is larger than bottom contact thickness),

$$\bar{R}_{c0}\left(\frac{r_{lp}}{t_{bc}}\right) = 0.295 + 0.037\left(\frac{r_{lp}}{t_{bc}}\right)^{-1} + 0.0595\left(\frac{r_{lp}}{t_{bc}}\right)^{-2}$$

$$\Delta\left(\frac{r_{lp}}{t_{bc}}\right) = 0.0409x^4 - 0.1015x^3 + 0.265x^2 - 0.0405x + 0.1065$$

where $x = \ln\left(\frac{r_{lp}}{t_{bc}}\right)$.

For both cases,

$$\beta\left(\frac{r_{lp}}{t_{bc}}\right) = 0.0016\left(\frac{r_{lp}}{t_{bc}}\right)^2 + 0.0949\left(\frac{r_{lp}}{t_{bc}}\right) + 0.6983$$

For the laser whose geometry is listed in Table 1, $\frac{r_{lp}}{t_{bc}} = \frac{431}{135} = 3.2$, which yields $\bar{R}_{c0} = 0.312$, $\Delta = 0.333$, and $\beta = 0.715$, leading to $\bar{R}_c = 0.64$ using the expressions above. Therefore, the second term in Equation 5, the contribution to the bottom contact resistance by the region just below the laser pedestal, is 23 Ω. This is small compared to the first term of Equation 5, the contribution by the rest of the bottom contact, which is 282 Ω. Since in most nanolaser geometries $r_{bc} \gg r_{lp}$, the first term of Equation 5 will be much larger than the second term. In our thermal simulation in Section 4, we distribute the total resistance from both terms of Equation 5, 305 Ω, across the entire bottom contact layer. For greater accuracy, the resistive heating resulting from the second term can be modeled as located directly beneath the laser pedestal, while the resistive heating resulting from the first term can be distributed across the rest of the bottom contact.

The Joule heat sources for our example nanolaser are listed at the left of Figure 3, and contribute a total of 0.226 mW of heating power to the nanolaser. The largest source of Joule heating is the lower pedestal, followed by the bottom contact. The bottom contact is expected to contribute negligibly to laser heating, since the intensity of heat generated is low, and the heat can easily flow out of this region into the substrate and bottom contact wire. Similarly, the lower pedestal is adjacent to the bottom contact, which can easily remove heat from the laser pedestal. Compared to the other heating sources shown in Figure 3, Joule heating is a minor contribution to laser self-heating.

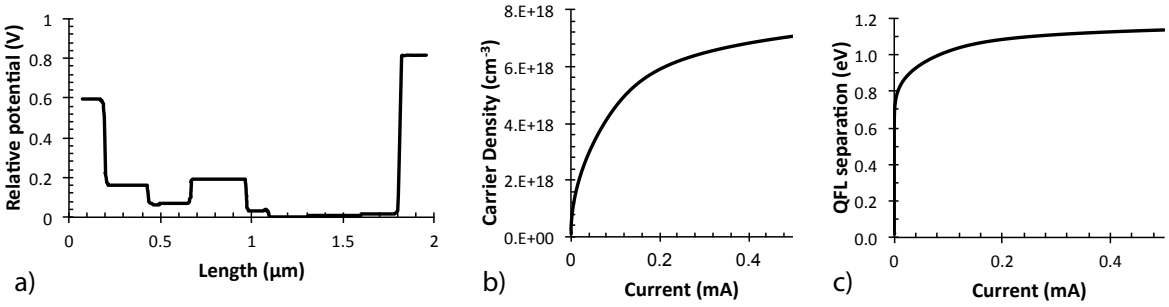

Figure 2.
Result of electronic simulation. (a) Potential difference as a function of vertical distance from the top of the top contact. Length = 0 corresponds to the top of the top contact layer, and length = 1.88 μm corresponds to the bottom of the bottom contact layer. (b) Carrier density as a function of injection current. (c) Quasi Fermi level (QFL) separation as a function of injection current.

3.2 Junction heating

Junction heating is the heat generated by the voltage change at the junction between the undoped gain layer and the adjacent doped semiconductor layers. To calculate the voltage changes, the device's electrical behavior should be simulated; we use SILVACO's ATLAS to calculate voltage, carrier density, and quasi-Fermi level separation. Using the voltage change V_{jn} at the nth junction, the power dissipated will be $P_{jn} = I_{th}V_{jn}$, where I_{th} is the laser threshold operating current.

For the laser described in Figure 1 and Table 1, the device voltage, carrier density, and I-V curve are shown in Figure 2 (a), (b), and (c), respectively. The potential difference at each junction between differently-doped layers is visible in Figure 2 (a). For this example we use a threshold current of $I_{th} = 0.4$ mA and a slightly larger operating current of $I = 0.5$ mA, which were experimentally used for a fabricated nanolaser with dimensions similar to this example.

Figure 3 lists the calculated junction heating sources for this laser, located at junctions 3 and 4 (all other junctions in the laser contribute to heterojunction heating instead, as described in Section 3.3). Together these two junctions contribute 0.110 mW of self-heating.

3.3 Heterojunction heating

Similar to junction heating, heterojunction heating is the heat generated by the voltage change at the remaining junctions, between the doped semiconductor layers. As before, the power dissipated at the nth junction is $P_{jn} = IV_{jn}$. This time, the current used is the operating current, rather than threshold current.

Figure 3 lists the calculated heterojunction heating sources for the laser described in Figure 1 and Table 1. Heterojunction heating adds 0.678 mW of self-heating to the laser. Most of this heating, however, takes place at the junction between the pedestals and the top or bottom contacts, and is easily dissipated via the contacts.

3.4 Surface recombination heating

Surface recombination is an additional heating term that is not usually considered for larger lasers, but becomes important for small lasers, for which the ratio of surface area to volume is large. The rate of surface recombination U_s in the gain region is given by

$$U_s = \frac{n}{\tau_s} \tag{6}$$

where n is carrier density (from the electronic simulation described in Section 3.2) and τ_s is carrier lifetime.[3] The carrier lifetime is given by

$$\frac{1}{\tau_s} = \frac{A_{active}}{V_{active}} v_s \tag{7}$$

where A_{active} and V_{active} are the area and volume of the gain region, and v_s is the surface recombination velocity. To calculate v_s at 300K for InGaAs, we use the value of v_s at 77K, $v_s = 6.7 \times 10^3 cm/s$, along with the knowledge that the v_s is proportional to the square root of temperature.[3] Thus, at 300K,

$$v_s(300K) = v_s(77K)\frac{\sqrt{300}}{\sqrt{77}} = 1.3 \times 10^4 cm/s \tag{8}$$

Using the above calculations to get the surface recombination rate U_s, we can then use our simulation of the quasi-Fermi level (QFL) from Figure 2(c) to calculate the heating power generated from surface recombination,

$$P_s = U_s \cdot V_{active} \cdot QFL \tag{9}$$

For our example nanolaser operating at T=300 K and at injection current I=0.5 mA, we calculate a QFL separation of 1.14 eV and a carrier concentration of 7.07e18 cm^{-3}. Using Equation 9, the surface recombination heating is calculated to be 0.393 mW.

3.5 Auger recombination heating

The last heating source we consider is Auger recombination[18] which, like the surface recombination heating, becomes a source of heat in the gain region. The Auger recombination rate U_A is given by

$$U_A = An^3 V_{active} \tag{10}$$

where n is the carrier density, V_{active} is the volume of the gain region, and A is the Auger coefficient. For InGaAs at 300K, the Auger coefficient is $9.8 \times 10^{-29} cm^6/s$.[18]

Using the carrier density for our example MCSEL at an injection current of 0.5 mA as calculated in Figure 2(b), we calculate the Auger recombination rate U_A to be $1.075 \times 10^{16} s^{-1}$. The Auger heating is then calculated as

$$P_A = U_A \cdot QFL$$

which yields 1.963 mW. This is by far the largest source of self-heating for the nanolaser, and because this heat source is located in the middle of the semiconductor stack, will also be the most difficult to dissipate.

In Figure 3 we summarize the self-heating sources for the example MCSEL and show their locations in the semiconductor stack. The junction and heterojunction heating sources are implemented as area heating sources located at the interfaces between layers, while Joule, surface recombination, and Auger recombination heating are volume heating sources implemented as distributed within each semiconductor layer. Only half of the device cross-section is shown since the device is approximated to be axially symmetric.

Note that each of these heat sources is dependent on operating temperature and on injection current. For the most accurate reflection of nanolaser temperature behavior, these heat sources should be updated to reflect the changing temperature as the nanolaser self-heats.

4. HEAT DISSIPATION

Once the sources of laser self-heating are known, the next step toward calculating laser operating temperature is to model the heat transport and dissipation in the laser. Heat transport heavily depends on the thermal parameters of the laser's constituent materials; thermal parameters for the materials used in the example MCSEL nanolaser, as well as a few other common nanolaser materials, are tabulated in Table 2. The values reported for amorphous aluminum oxide ($\alpha - Al_2O_3$) are for material deposited via atomic layer deposition (ALD). The range of thermal conductivities represents the range of values found in the literature[19–21] for $\alpha - Al_2O_3$. For all these materials, the thermal (and optical) parameters depend on the deposition conditions, so for the best accuracy, they should be measured for each new deposition recipe.

In addition to the heat sources and thermal parameters, another important factor affecting laser operating temperature are the device's heat dissipation capabilities. Depending on the experimental setup, heat may be

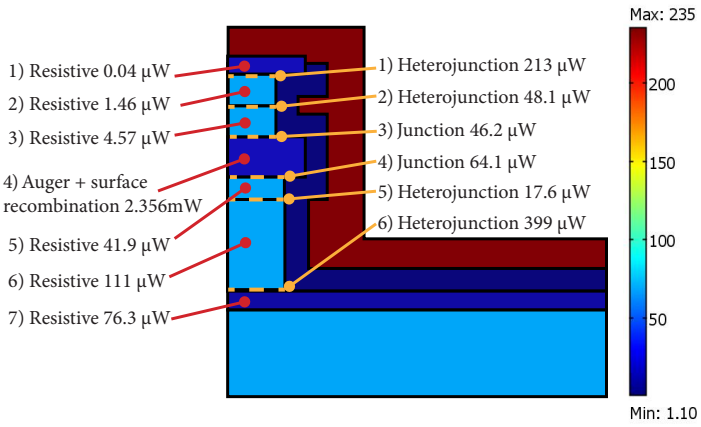

Figure 3.
Amount and location of heating sources in the example MCSEL laser, at 300K ambient temperature and 0.5mA operating current. Each region is colored according to its thermal conductivity at 300K.

Table 2.
Thermal parameters used in heat transport simulations of the example MCSEL. All values are reported for T=300K.

	$\alpha - Al_2O_3$ (ALD)	SiO_2 (PECVD)	InP	$In_xGa_{1-x}As$ $x = 0.53$	$In_xGa_{1-x}As_yP_{1-y}$ $x = 0.773,\ y = 0.493$	Ag
Thermal conductivity k $\left(W \cdot m^{-1} \cdot K^{-1}\right)$	1.7-20[19–21]	1.1[22]	68[16]	16[23]	11[15]	429[24]
Heat capacity Cp $\left(J \cdot kg^{-1} \cdot K^{-1}\right)$	880[21]	725[25]	310[16]	320[15]	320[15]	235[26]
Density $\rho\ \left(kg \cdot m^{-3}\right)$	3690[21]	2200[27]	4810[16]	5500[15]	5120[15]	10490[26]

dissipated through the sample's substrate into a heat sink (with the quality of heat transfer dependent on the thermal contact between substrate and heat sink) or through the electrical contact wires, or to the surrounding air via radiation or convection. In our simulation we allow for both these situations, with the contact wires and substrate bottom approximated as perfect heat sinks. Figure 4 shows the boundary conditions for our thermal simulation, which define the locations and mechanisms of heat dissipation.

We model the heat transport in this MCSEL nanolaser using COMSOL's 2D axial-symmetric steady-state heat conduction model. In our case, we directly model the steady-state laser operating temperature, assuming that the temperature rise will be moderate and the temperature dependences of the heat sources and thermal parameters are relatively small. For the most accurate simulation, especially in the case where temperature change and/or temperature dependence is large, the temperature should be iteratively solved and the heating sources and material parameters adjusted at each time step. The results of our steady-state simulation are found in Figure 5, with temperature represented as color, and heat flux magnitude and direction represented by arrows.

From these results, we see that the mechanism of heat dissipation depends strongly on the dielectric shield's thermal conductivity. For higher-conductivity shields (Figure 5 (a)), the laser can dissipate heat through the shield layer, while for lower-conductivity shields (Figure 5 (b)), the primary method of laser heat transfer is through the InP upper and lower pedestals. By setting each boundary in turn to insulation, we determined that once the heat leaves the laser cavity, the most significant avenue for heat dissipation is conduction through the metal shield. In the higher-conductivity case, the laser's steady-state operating temperature is a maximum of 324 K, which occurs in the center of the gain region. In the lower-conductivity case, the laser heats to a maximum of 353 K, with the heat less able to escape from the edges of the gain region.

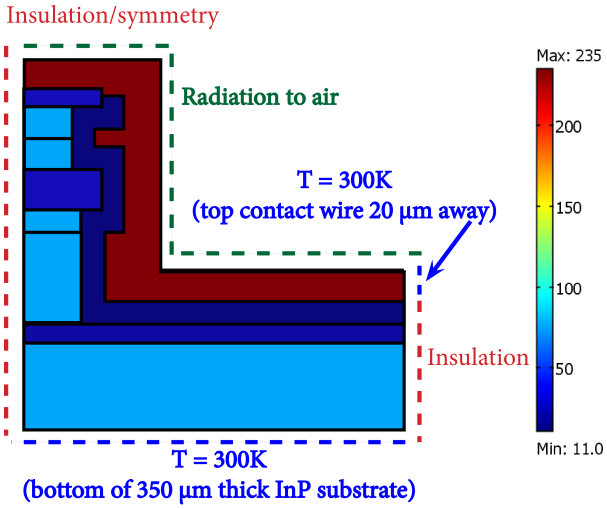

Figure 4.

Boundary conditions used in heat transport simulation. The laser is simulated as a 2D axially-symmetric structure; the left edge is the axis of symmetry. The top surface of the metal cladding is surrounded by air, and is allowed to dissipate heat to ambient through radiation. The InP substrate is 350 μm thick (full thickness included in the model but not shown here), the bottom of which is set to a constant temperature of 300 K. This represents a perfect heat sink at the substrate bottom. Another perfect heat sink is located at the far right edge of the metal cladding, 20 μm away (again, full distance included in the model but not shown here); this represents heat conduction through the top contact wire. The rest of the simulation's right edge is set to insulation, since the right edge of the substrate is much farther away than the top contact wire and, because this surface faces air, is assumed to contribute negligibly to heat dissipation.

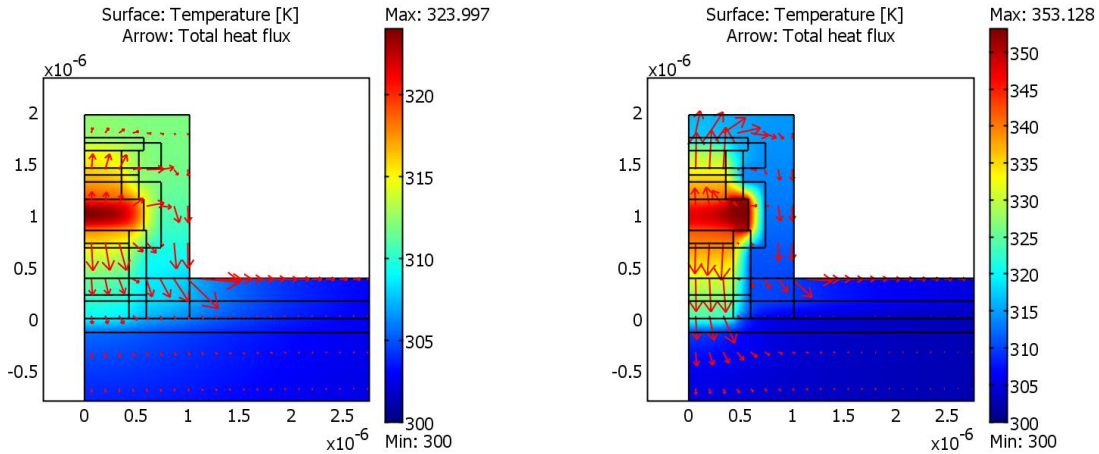

Figure 5.

Calculated steady-state operating temperature of the MCSEL at 0.5 mA injection current and 300 K ambient temperature. Arrows represent the direction of heat flux, with the length of the arrow representing the amount of heat flux. Here, the dielectric shield is (a) $\alpha - Al_2O_3$ with thermal conductivity of k = 20 $W \cdot m^{-2} \cdot K^{-1}$, the highest literature value reported, or (b) SiO_2 with thermal conductivity of k = 1.1 $W \cdot m^{-2} \cdot K^{-1}$, also comparable to the lowest literature value reported for ALD $\alpha - Al_2O_3$ (Table 2).

5. DISCUSSION

Simulation of nanolaser operating temperature is important in the diagnosis of laser thermal problems, as well as in identifying design changes that may improve nanolaser thermal performance. Here, we demonstrated an example thermal model by calculating the magnitudes and locations of self-heating sources in a nanolaser, and simulating heat transport. We recognize that further improvements in the accuracy of MCSEL thermal models will increase their usefulness, as well as reveal the nanolasers' temperature-dependent dynamics.

One significant improvement could be made by incorporating thermal feedback. For example, this basic model assumed a relatively modest temperature rise that does not significantly affect the laser's carrier density or material parameters. In the future, a self-consistent solution including the interdependences of self-heating sources and thermal parameters on laser's operating temperature, such as in VCSELs,[12] will more fully reflect the true operating temperature and temperature-dependent dynamics.

The thermal parameters of nanolaser materials vary not only with temperature, but also with fabrication recipe. For the most experimentally-relevant models, these thermal parameters should be experimentally measured for each fabrication recipe. This measurement can be performed with the 3ω method[28] , which has been adapted to measure thermal conductivity in solids[28] and thin films,[29,30] as well as across junctions.[31] Another alternative is scanning thermal microscopy, which has been used to measure thermal conductivities and probe the local temperatures of nanoscale structures.[32,33] When combined with high-sensitivity bi-material cantilevers, very high spatial and thermal resolution may be achieved.[32,34] Such high-resolution measurements may provide experimental validation of nanolaser thermal models.

In addition, the use of nanoscale heat transport models, rather than macroscale, should be investigated for these nanolasers. Although the few MCSEL thermal studies that exist have used macroscale heat transfer,[35] the dimensions of these nanolasers are comparable to the phonon mean free paths in many of their constituent materials, putting them in the nanoscale heat transfer regime.[36] We are currently expanding our model to include nanoscale heat transport, including an analysis of the circumstances under which the difference between macroscale and nanoscale heat transport become significant.

ACKNOWLEDGMENTS

The authors would like to thank Dr. Boris Slutsky and Mr. Dor Gabay for helpful discussions. This work was supported by the Defense Advanced Research Projects Agency (DARPA), the National Science Foundation (NSF) through the Center for Integrated Access Networks (CIAN) NSF ERC under grant #EEC−0812072, the Cymer Corporation, the Office of Naval Research MURI program, and the U.S. Army Research Office. This work was also partly supported by the Brazilian financial agencies: FAPESP, CNPQ, CAPES and done within the National Institute for Science and Technology (FOTONICOM) and the Center for Optics and Photonics (CePOF).

REFERENCES

1. J. H. Lee, M. Khajavikhan, A. Simic, Q. Gu, O. Bondarenko, B. Slutsky, M. P. Nezhad, and Y. Fainman, "Electrically pumped sub-wavelength metallo-dielectric pedestal pillar lasers," *Optics Express* **19**, pp. 21524–21531, Oct. 2011.
2. K. Ding and C. Z. Ning, "Fabrication challenges of electrical injection metallic cavity semiconductor nanolasers," *Semiconductor Science and Technology* **28**, p. 124002, Nov. 2013.
3. M. T. Hill, Y.-S. Oei, B. Smalbrugge, Y. Zhu, T. de Vries, P. J. van Veldhoven, F. W. M. van Otten, T. J. Eijkemans, J. P. Turkiewicz, H. de Waardt, E. J. Geluk, S.-H. Kwon, Y.-H. Lee, R. Nötzel, and M. K. Smit, "Lasing in metallic-coated nanocavities," *Nature Photonics* **1**, pp. 589–594, Sept. 2007.
4. M. P. Nezhad, A. Simic, O. Bondarenko, B. Slutsky, A. Mizrahi, L. Feng, V. Lomakin, and Y. Fainman, "Room-temperature subwavelength metallo-dielectric lasers," *Nature Photonics* **4**, pp. 395–399, Apr. 2010.
5. M. Khajavikhan, A. Simic, M. Katz, J. H. Lee, B. Slutsky, A. Mizrahi, V. Lomakin, and Y. Fainman, "Thresholdless nanoscale coaxial lasers," *Nature* **482**, pp. 204–207, Jan. 2012.
6. Q. Gu, B. Slutsky, F. Vallini, J. S. T. Smalley, M. P. Nezhad, N. C. Frateschi, and Y. Fainman, "Purcell effect in sub-wavelength semiconductor lasers," *Optics Express* **21**(13), p. 15603, 2013.

7. C. Z. Ning, "What is Laser Threshold?," *IEEE Journal of Selected Topics in Quantum Electronics* **19**, pp. 1503604–1503604, May 2013.
8. O. Hess, J. B. Pendry, S. A. Maier, R. F. Oulton, J. M. Hamm, and K. L. Tsakmakidis, "Active nanoplasmonic metamaterials," *Nature Materials* **11**, pp. 573–584, July 2012.
9. K. Ding, M. T. Hill, Z. C. Liu, L. J. Yin, P. J. van Veldhoven, and C. Z. Ning, "Record performance of electrical injection sub-wavelength metallic-cavity semiconductor lasers at room temperature," *Optics Express* **21**(4), pp. 4728–4733, 2013.
10. W. S. Hobson, U. Mohideen, S. J. Pearton, R. E. Slusher, and F. Ren, "SiN x/sulphide passivated GaAs/AlGaAs microdisk lasers," *Electronics Letters* **29**(25), pp. 2199–2200, 1993.
11. K. Ding and C. Z. Ning, "Metallic subwavelength-cavity semiconductor nanolasers," *Light: Science & Applications* **1**, p. e20, July 2012.
12. C. Z. Ning, R. A. Indik, and J. V. Moloney, "Self-consistent approach to thermal effects in vertical-cavity surface-emitting lasers," *JOSA B* **12**(10), pp. 1993–2004, 1995.
13. J. S. T. Smalley, Q. Gu, and Y. Fainman, "Temperature Dependence of the Spontaneous Emission Factor in Subwavelength Semiconductor Lasers," *IEEE Journal of Quantum Electronics* **50**, pp. 175–185, Mar. 2014.
14. S. F. Yu, *Analysis and design of vertical cavity surface emitting lasers*, Wiley - VCH, Jan. 2003.
15. N. M. Schmidt and Y. A. Goldberg, Handbook Series on Semiconductor Parameters *Volume 2: Ternary And Quaternary III-V Compounds* , vol. 2 of *Handbook Series on Semiconductor Parameters*, World Scientific, London, Jan. 1996.
16. N. M. Schmidt and Y. A. Goldberg, Handbook Series on Semiconductor Parameters *Volume 1: Si, Ge, C (Diamond), GaAs, GaP, GaSb, InAs, InP, InSb*, vol. 1 of *Handbook Series on Semiconductor Parameters*, World Scientific, London, Jan. 1996.
17. P. Zhang, Y. Y. Lau, W. Tang, M. R. Gomez, D. M. French, J. C. Zier, and R. M. Gilgenbach, "Contact resistance with dissimilar materials: bulk contacts and thin film contacts," in *Electrical Contacts (Holm), 2011 IEEE 57th Holm Conference on*, pp. 1–6, IEEE, Sept. 2011.
18. G. P. Agrawal and N. K. Dutta, *Semiconductor lasers*, Van Nostrand Reinhold, New York, Jan. 1993.
19. S. Yoneoka, J. Lee, M. Liger, G. Yama, T. Kodama, M. Gunji, J. Provine, R. T. Howe, K. E. Goodson, and T. W. Kenny, "Electrical and Thermal Conduction in Atomic Layer Deposition Nanobridges Down to 7 nm Thickness," *Nano Lett* **12**, pp. 683–686, Feb. 2012.
20. J. R. Wank, S. M. George, and A. W. Weimer, "Nanocoating individual cohesive boron nitride particles in a fluidized bed by ALD," *Powder Technology* **142**, pp. 59–69, Apr. 2004.
21. E. Dörre and H. Hübner, Alumina: processing, properties, and applications, Springer-Verlag, Berlin, Jan. 1984.
22. M. B. Kleiner, S. A. Kuhn, and W. Weber, "Thermal conductivity measurements of thin silicon dioxide films in integrated circuits," *Electron Devices, IEEE Transactions on* **43**(9), pp. 1602–1609, 1996.
23. S. Adachi, Physical Properties of III-V Semiconductor Compounds, John Wiley & Sons, Inc., Mörlenbach, Jan. 1992.
24. N. A. Lange, Lange's Handbook of Chemistry, McGraw-Hill Professional, 15 ed., Jan. 1999.
25. S. Andersson and L. Dzhavadov, "Thermal conductivity and heat capacity of amorphous SiO2: pressure and volume dependence," *Journal of Physics: Condensed Matter* **4**(29), p. 6209, 1992.
26. D. R. Lide, CRC Handbook of Chemistry and Physics, CRC Press, 84 ed., June 2003.
27. E. Bassous, "Fabrication of novel three-dimensional microstructures by the anisotropic etching of (100) and (110) silicon," *IEEE Transactions on Electron Devices* **25**, pp. 1178–1185, Oct. 1978.
28. D. G. Cahill, "Thermal conductivity measurement from 30 to 750 K: the 3ω method," *Review of Scientific Instruments* **61**(2), p. 802, 1990.
29. D. G. Cahill, M. Katiyar, and J. R. Abelson, "Thermal conductivity of alpha-Si:H thin films," *Physical Review B* **50**(9), p. 6077, 1994.
30. T. Borca-Tasciuc, A. R. Kumar, and G. Chen, "Data reduction in 3ω method for thin-film thermal conductivity determination," *Review of Scientific Instruments* **72**(4), p. 2139, 2001.
31. R. Y. Wang, R. A. Segalman, and A. Majumdar, "Room temperature thermal conductance of alkanedithiol self-assembled monolayers," *Applied Physics Letters* **89**(17), p. 173113, 2006.

32. A. Majumdar, "Scanning thermal microscopy," *Annual review of materials science* **29**(1), pp. 505–585, 1999.
33. K. Kim, W. Jeong, W. Lee, and P. Reddy, "Ultra-High Vacuum Scanning Thermal Microscopy for Nanometer Resolution Quantitative Thermometry," *ACS Nano* **6**, pp. 4248–4257, May 2012.
34. S. Shen, A. Henry, J. Tong, R. Zheng, and G. Chen, "Polyethylene nanofibres with very high thermal conductivities," *Nature Nanotechnology* , pp. 1–5, Mar. 2010.
35. Z. Liu, J. M. Shainline, G. E. Fernandes, J. Xu, J. Chen, and C. F. Gmachl, "Continuous-wave subwavelength microdisk lasers at $\lambda = 1.53\mu m$," *Optics Express* **18**, pp. 19242–19248, Aug. 2010.
36. T. Luo and G. Chen, "Nanoscale heat transfer – from computation to experiment," *Physical Chemistry Chemical Physics* **15**(10), pp. 3389–3412, 2013.